



An aptamer-based magnetic flow cytometer using matched filtering

Chih-Cheng Huang^a, Partha Ray^b, Matthew Chan^c, Xiahan Zhou^c, Drew A. Hall^{c,d,*}

^a Materials Science and Engineering Program, University of California – San Diego, La Jolla, CA, 92093, USA

^b Division of Surgical Oncology, Department of Surgery, Moores Cancer Center, UC San Diego Health, La Jolla, CA, 92093, USA

^c Department of Electrical and Computer Engineering, University of California – San Diego, La Jolla, CA, 92093, USA

^d Department of Bioengineering, University of California – San Diego, La Jolla, CA, 92093, USA

ARTICLE INFO

Keywords:

Aptasensor
Flow cytometry
Magnetic biosensor
Matched filtering
Pancreatic cancer
Point-of-Care (PoC) testing

ABSTRACT

Facing unprecedented population-ageing, the management of noncommunicable diseases (NCDs) urgently needs a point-of-care (PoC) testing infrastructure. Magnetic flow cytometers are one such solution for rapid cancer cellular detection in a PoC setting. In this work, we report a giant magnetoresistive spin-valve (GMR SV) biosensor array with a multi-stripe sensor geometry and matched filtering to improve detection accuracy without compromising throughput. The carefully designed sensor geometry generates a characteristic signature when cells labeled with magnetic nanoparticles (MNPs) pass by thus enabling multi-parametric measurement like optical flow cytometers (FCMs). Enumeration and multi-parametric information were successfully measured across two decades of throughput (37 — 2730 cells/min). 10- μ m polymer microspheres were used as a biomimetic model where MNPs and MNP-decorated polymer conjugates were flown over the GMR SV sensor array and detected with a signal-to-noise ratio (SNR) as low as 2.5 dB due to the processing gain afforded by the matched filtering. The performance was compared against optical observation, exhibiting a 92% detection efficiency. The system achieved a 95% counting accuracy for biomimetic models and 98% for aptamer-based pancreatic cancer cell detection. This system demonstrates the ability to perform reliable flow cytometry toward PoC diagnostics to benefit NCD control plans.

1. Introduction

Noncommunicable diseases (NCDs), generally known as chronic diseases, have become the primary risk of death with unprecedented population-ageing (United Nations, 2017). According to the World Health Organization (WHO), more than 80% of deaths are caused by NCDs in countries where at least 20% of the population is over 60 years old (World Health Organization, 2018). Inevitably, the growing impact of NCDs necessitates changes to the contemporary healthcare system that was designed many decades ago. While the successful transformation requires management of common NCDs (e.g., cancers, cardiovascular diseases, diabetes, etc.), it is predicated on effective diagnosis, screening, monitoring, and treatment. The upcoming digital-health era shifts healthcare from a sick-care response to a proactive system with personalized medicine that addresses many unmet needs of NCD management (Bhavnani et al., 2016; Li et al., 2017; Wannenburg and Malekian, 2015).

One of the key factors to enable the unbridled ubiquity of digital health is to transition diagnostics from centralized laboratories closer to

the patient in point-of-care (PoC) settings. PoC settings integrated with health information technology, telemedicine, and portable testing provide high effectiveness, low cost, easy access, and fast turnaround. Many technologies have improved the feasibility of PoC testing using optical biosensors (Kwon et al., 2016; Zhu et al., 2013), FET-based biosensors (Afsahi et al., 2018; Wang et al., 2014), electrochemical biosensors (Aronoff-Spencer et al., 2016; Jiang et al., 2017; Sun and Hall, 2019), and magnetic biosensors (Zhou et al., 2019a, 2019b), amongst many others. PoC diagnostics offers timely detection and treatment monitoring of cancers where early detection has a huge impact on the treatment outcome and survival rate while simultaneously reducing the economic burden. Optical-based instrumentation is still the workhorse in clinical diagnostics with techniques such as flow cytometry. A flow cytometer (FCM) is an essential tool in hematology for quantitative analysis of cells with applications including identifying prognostic indicators of cancer, HIV, and other time-dependent biomarkers of disease activity (Jennings and Foon, 1997; Perfetto et al., 2004; Malcovati et al., 2007). A cellular collection system can be added to realize fluorescence-activated cell sorting (FACS) for high throughput and

* Corresponding author. Department of Electrical and Computer Engineering, University of California – San Diego, La Jolla, CA, 92093, USA.
E-mail address: drewhall@ucsd.edu (D.A. Hall).

multi-parameter, quantitative cellular analysis and sorting (Julius et al., 1973). However, such instrumentation requires complex optics, lasers, and photodetectors making it hard to translate to the PoC. CMOS-based optical biosensors have integrated the necessary components into portable formats (Vashist et al., 2015; Zhu et al., 2013, 2011); however, the devices still fall short of the PoC promise due to the need for extensive sample pretreatment and bulky optics that require alignment and/or calibration.

To address cancerous cell detection for NCD control, a magnetic flow cytometer (MFC) provides an alternative platform for the multi-parametric quantification of cellular information while molding PoC-friendly settings like rapid turnaround time and miniaturization without the loss of sensitivity (Helou et al., 2013; Huang et al., 2017a,b; Issadore et al., 2012; Lin et al., 2016; Loureiro et al., 2011; Murali et al., 2016; Reisbeck et al., 2018, 2016; Tang et al., 2019, 2019; Zhou et al., 2017). Magnetic biosensing approaches replace the fluorescent (or colorimetric) label with a magnetic tag. Magnetic detection has less background noise than optical measurements where issues such as photobleaching and auto-fluorescence are always present requiring sample pretreatment to remedy (Cossarizza et al., 2017; Salvati et al., 2018; Williams et al., 2017). Thus, magnetic sensing simplifies the assay procedure by greatly easing the necessary sample preparation (Fernandes et al., 2014b Freitas et al., 2012; Gaster et al., 2009; Osterfeld et al., 2008; Rizzi et al., 2017; Wang et al., 2015).

In this work, we developed a giant magnetoresistive spin-valve (GMR SV)-based MFC using matched filtering and a multi-stripe sensor geometry to improve detection accuracy (Fig. 1). At a high level, the system can be explained as follows: when an analyte (e.g., a cancer cell) labeled with magnetic nanoparticles (MNPs) flows over the sensor, a change in resistance of the underlying sensor is induced. The carefully designed sensor layout creates a characteristic signature from MNPs, as shown in Fig. 1B, thus enabling multi-parametric measurement like optical FCMs. An array of sensors spaced along the fluidic channel extract the time-of-flight (ToF), which can be used as a proxy for the size and hydrodynamic volume of the cell. To study this effect, we have done a full force vector analysis and studied the effect of different MNP sizes and flow cell dimensions. Enumeration and multi-parametric information were successfully measured across two decades of throughput. Biomimetic constructs consisting of 10- μm polymer microspheres were used as a model system where MNPs and MNP-decorated polymer conjugates were flown over the GMR SV sensor array and detected with a signal-to-noise ratio (SNR) as low as 2.5 dB due to the processing gain afforded by the matched filtering. The matched-filtering results were compared with optical observation, showing correlation rates up to 92%. The GMR SV-based MFC achieves 95% counting accuracy in the

biomimetic sample (MNP-decorated polymer spheres). We then designed a high affinity aptamer towards epidermal growth factor receptor (EGFR) and showed detection of a pancreatic cell line (Panc-1) with 98% correlation to an optical FCM. This is the first work to use aptamers in an MFC and demonstrates the ability to perform reliable PoC diagnostics towards the benefit of NCD control plans.

2. Materials and Methods

2.1. Magnetic flow cytometer

The MFC consisted of a GMR SV chip (MagArray), a NdFeB permanent magnet, a microfluidic channel, and electrical readout circuitry (Supplemental Fig. 1). Each GMR SV chip has 80 individually addressable sensors arranged in an 8×10 matrix where each sensor is $120 \times 120 \mu\text{m}^2$ on a $280 \mu\text{m}$ pitch with a nominal resistance (R_0) of 1464Ω and a mean magnetoresistance (MR) ratio of 7.99% (Supplemental Fig. 2). Only one row of sensors ($n = 8$) was used in this work. The NdFeB permanent magnets (K&J Magnetics, B881, B882, B882-N52, BCC2, or BCC2-N52) were mounted horizontally 4.5 mm below the sensor chip with an out-of-plane field that ranged from 0.06 to 0.13 T, as measured by a gaussmeter (Lake Shore Cryotronics, 475DSP).

The GMR SV sensors were read out using lock-in detection excited by a 1 V_{pp} sinusoidal source at 7 kHz generated by a data acquisition card (National Instruments, PCIe-6361), as shown in Supplemental Fig. 3. The resulting current was amplified by a transimpedance amplifier (TIA) implemented using an OpAmp (Analog Devices, AD8655) with resistive feedback ($R_F = 42.2 \text{ k}\Omega$). A bleed resistor ($R_B = 1.5 \text{ k}\Omega$) was used to cancel the non-magnetoresistive portion of the current and avoid saturating the TIA, thus enabling the gain to be increased by 28 dB. Eight parallel channels of this circuit were assembled on a custom printed circuit board (PCB). The TIA outputs were sampled at 125 kSps/ch. and processed in LabVIEW using a Fast Fourier Transform (FFT) to demodulate the signal (125-point FFT, 1 ms acquisition time). The input-referred noise of the system was measured to be $4.2 \text{ m}\Omega_{\text{RMS}}$ and spectrally white (Supplemental Fig. 4).

Optical measurements were taken by an optical microscope (Motic, #BA310MET-T) with a microscope camera (Moticam, #1080) or a lens-mounted mobile phone (iPhone X) for video recording under different flow rates. The videos were post processed with a monochromatic filter and magnetic analytes were enumerated using a custom written MATLAB code via size thresholding.

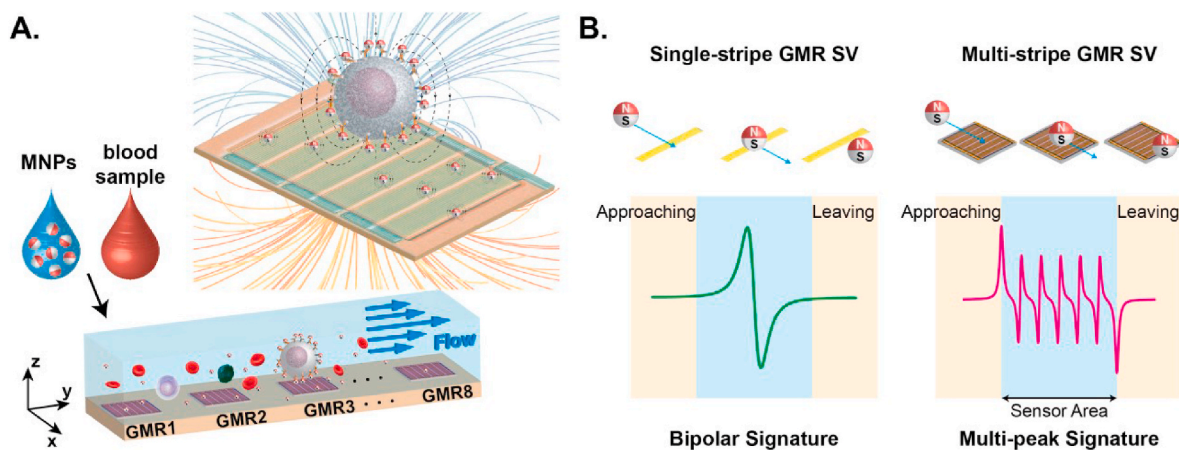


Fig. 1. Magnetic flow cytometer (MFC) concept: **A.** Operation of a GMR SV-based MFC where MNP decorated cells flow over GMR SV sensors. **B.** Signature from conventional single-stripe sensors with a simple bipolar-peak which increases the false detection events and the proposed multi-stripe configuration that enhances the signal differentiation by creating a unique magnetic signature.

2.2. Microfluidics

Microfluidic channels were fabricated using a standard poly(dimethylsiloxane) (PDMS) process with SU-8 molding and PDMS curing with channel widths ranging from 90 to 120 μm and heights ranging from 14 to 40 μm . GMR SV chips were placed in a UV-ozone chamber (UVO-TECH, HELIOS-500) for 15 min prior to bonding with the PDMS microfluidic channels. The microfluidic chips were subsequently aligned and cured for 1 h at 75 °C. The inlet and outlet of the PDMS channels were mechanically drilled and connected to a syringe pump (NE-300, New Era Pump Systems) with poly(tetrafluoroethylene) (PTFE) tubing.

2.3. Magnetic nanoparticles

Superparamagnetic MNPs, Dynabeads M-450 (Invitrogen, #14011), Dynabeads M-280 (Invitrogen, #11205D), Bio-Adembeads (Ademtech, #03121), and SHS-30 (Ocean NanoTech, #SHS-30-01), were used in all experiments with hydrodynamic diameters of 4.5 μm , 2.8 μm , 200 nm, and 40 nm, respectively. Dynabeads M-450 and Dynabeads M-280 with a core particle size of 7.7 nm were washed 3 \times with 0.1 \times PBS before resuspending in 1 mL buffer at dilutions of 1:400 and 1:650 ($1.0 \times 10^6 \text{ mL}^{-1}$), respectively. A nonionic surfactant, 0.05% of Tween 20 (Sigma-Aldrich, #P1379), was added to the diluted Dynabeads solution. Streptavidin-coated Bio-Adembeads and SHS-30 were centrifuged each time before washing (the same procedure as the Dynabeads); the final dilution ratios were 1:20 ($4.2 \times 10^{10} \text{ mL}^{-1}$) and 1:1 ($2.0 \times 10^{13} \text{ mL}^{-1}$), respectively.

2.4. Hydrodynamic analysis

Hydrodynamic forces were calculated to determine the optimal channel height and magnetic field (De Palma et al., 2007; Liu et al., 2009; Wirix-Speetjens et al., 2005). Forces acting on a MNP included the drag force (F_D), magnetic force (F_M), gravity (F_G), and DLVO forces (Van der Waals force (F_{VDW}) and electro-repulsive force (F_{el})), and Langevin force (F_{lang}), as shown in Supplemental Fig. 5. The drag force is calculated as

$$F_D = -6\pi\eta C_D R_p (v_p - v_m) \quad (1)$$

where η is the viscosity of the medium, C_D is the drag coefficient defined by the MNP size and shape, R_p is the MNP radius, v_p is the MNP's velocity, and v_m is the medium velocity. The magnetic force is calculated as

$$F_M = \frac{(\chi - \chi_m)V_p(\mathbf{B} \cdot \nabla \mathbf{B})}{\mu_0} \quad (2)$$

where χ is the volume susceptibility (dimensionless), χ_m is the medium's volume susceptibility, V_p is the MNP volume, \mathbf{B} is the magnetic flux density, and μ_0 is the permeability of free space. Gravity is calculated as

$$F_G = (\rho_p - \rho_m)V_p g \quad (3)$$

where ρ_p is the MNP density, ρ_m is the medium density, and g is the gravitational acceleration. Van der Waals, electro-repulsive and Langevin forces are calculated by

$$F_{VDW} = -\frac{AR_p}{6d^2} \quad (4)$$

$$F_{el} = \frac{2\pi\epsilon_0\epsilon_r}{1 - e^{-2kd}} \left[2\psi_p\psi_s e^{-kd} + (\psi_p^2 + \psi_s^2) e^{-2kd} \right] \quad (5)$$

$$F_{lang}^2(f) = 6\pi k_B T \eta C_D R_p \quad (6)$$

where A is Hamaker constant, d is the distance between MNPs or between the MNP and sensor, ϵ_0 is the permittivity of free space, ϵ_r is the relative permittivity, ψ_p is the MNP surface potential, ψ_s is the sensor

surface potential, κ is the Debye-Hückel length, k_B is the Boltzmann constant, and T is the temperature (in Kelvin). Custom written MATLAB code was used to calculate the resulting forces based on Eqs. (1)–(6).

2.5. Biomimetic polymer microspheres

Biotin-coated 10- μm polymer microspheres, ProActive CP10N (Bangs Laboratories, #CP10000), were conjugated with Bio-Adembeads to create a biomimetic construct used during algorithm development and evaluation. To build such construct, an aliquot of ProActive CP10N was washed with 10 \times volume of wash buffer (0.1 \times PBS + 0.05% Tween20, pH = 7.4) three times. The pellet in the wash buffer was resuspended with 1:20 dilution. The diluted Bio-Adembeads (1:20) were added to this solution. The magnetic conjugates were formed and incubated at room temperature (18–25 °C) for 30 min with gentle mixing. The sample was resuspended in 20 \times volume of wash buffer prior to injecting into the microfluidic channel using a syringe pump (New Era Pump Systems, NE-1000).

2.6. Micromagnetic modelling

The Stoner-Wohlfarth model was used for magnetic modelling (Li and Wang, 2003). MNPs are assumed to be Langevin spheres in the field, have a linear superparamagnetic response, and give rise to dipole fields. Here, we considered only the spatially averaged magnetic field emanated from a single MNP being magnetized by the applied field (H_A). Thus, the average field that acts on the free layer of the GMR SV sensor ($\overline{H_s}$) is:

$$\overline{H_s} = \frac{1}{lwt} \int_{-\frac{l}{2}}^{\frac{l}{2}} \int_{-\frac{w}{2}}^{\frac{w}{2}} \int_{-\frac{t}{2}}^{\frac{t}{2}} \frac{\chi R_p^3}{3} \left[\frac{3(\mathbf{H}_A \cdot \mathbf{r})\mathbf{r}}{r^5} - \frac{\mathbf{H}_A}{r^3} \right] dx dy dz \quad (7)$$

where l is the sensor length, w is the sensor width, t is the free layer thickness, H_A is the applied magnetic field, r is the distance between the MNP (x_0, y_0, z_0) and the point of free layer (x, y, z), x and y are the in-plane axes, and z is the out-of-plane axis, as shown in Fig. 2A. It is assumed that H_A points in the z -direction without divergence of the in-plane component and the $\overline{H_s}$ component along the long-axis (x , in Fig. 1A) is neglected due to the sensor's insensitivity to the long-axis field. Consequently, the average field along the short-axis, y , is:

$$\langle \mathbf{H}_s \rangle_y = \frac{\chi H_A R_p^3}{lwt} \int_{-\frac{l}{2}}^{\frac{l}{2}} \int_{-\frac{w}{2}}^{\frac{w}{2}} \int_{-\frac{t}{2}}^{\frac{t}{2}} \left[\frac{(y - y_0)(z - z_0)}{r^5} \right] dx dy dz \quad (8)$$

All micromagnetic simulations, such as those shown in Fig. 2, were performed using custom written MATLAB code implementing Eq. (8).

2.7. Signal processing

Cross-sensor correlation and matched filtering were applied on the acquired data to calculate the time-of-flight (ToF) across the sensor array and improve the SNR, respectively. Cross-sensor correlation involves convolving a signal segment from a detected event with the signal measured on a downstream sensor (*i.e.* using the signature observed on Sensor 1 or Sensor 2). The resulting signal is thresholded to find the time position of the connected event and the ToF is calculated based on the known sensor-sensor spacing and time difference. Matched filtering convolves the measured signal with a template. Three different templates were evaluated with matched filtering: simulation-based matched filters (SMF), energy-detection matched filters (EDMF), and previous-event matched filters (PEMF). The SMF utilizes Eq. (8) to generate a library of templates. The EDMF template quantizes the expected signature into a tertiary square waveform. Lastly, the PEMF relies on the signature detected at a previous sensor. These templates are illustrated in Supplemental Fig. 6. All signal processing was performed in MATLAB using custom written code.

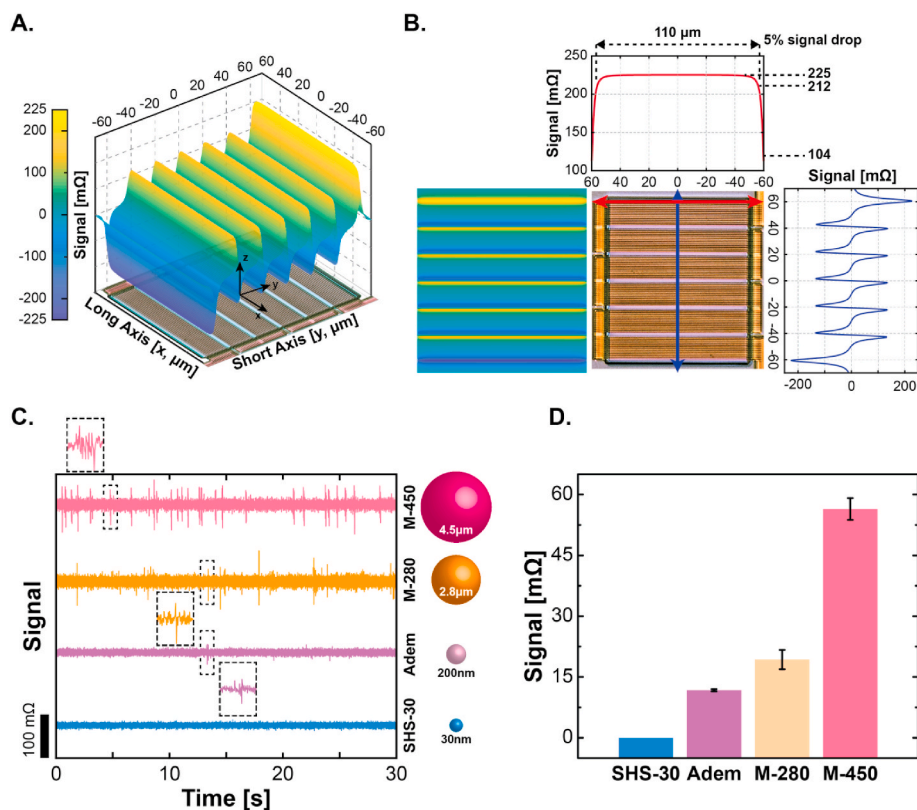


Fig. 2. Simulation and measurement results for MNPs passing over a magnetic sensor. **A.** 3D illustration of simulated signal. **B.** Simulated 2D profile of positional signal dependence. **C.** Measurement of different MNPs and their magnetic signatures under the same flow rate. **D.** Plot of measured signal amplitude vs. MNP size.

2.8. Aptamer-based MFC assay

Panc-1 and MiaPaCa-2 pancreatic cancer cell lines were grown to 80% confluence in Dulbecco's modified Eagle medium (DMEM) (Gibco, #11965084) with 10% fetal bovine serum (FBS) (Gibco, #26140079) and 1% penicillin/streptomycin (Gibco, #15070063). The adherent cells were treated with Trypsin (Gibco, #25300062) to detach them from the tissue culture flask using standard cell culture techniques. The cell viability and the size were calculated using a Vi-CELL XR Cell Viability Analyzer (Beckman Coulter). The cells were finally washed and resuspended in PBS/MgCl₂/CaCl₂ (Gibco, #14040133) for the assay.

The 5'-biotinylated-E07 (anti-EGFR aptamer) was generated by performing an *in vitro* transcription reaction (DuraScribe T7 Transcription Kit, Lucigen, #DS010925), as described previously (Ray et al., 2012). 5'-Biotin-G-Monophosphate (TriLink, #N-6003) at a 20 mM (final concentration) was also added to the reaction mixture for the incorporation of 5'-biotin to the E07 aptamer (Bompiani et al., 2012). The transcribed 5'-biotinylated E07 aptamer was purified by denaturing poly acrylamide gel electrophoresis (PAGE). A biotinylated anti-EGFR antibody (R&D systems, #FAB9577B-100) was also used for comparison.

The cells ($\sim 3 \times 10^5$) were incubated with the 5'-biotinylated E07 aptamer at a final concentration of 100 nM in 100 μ L PBS/MgCl₂/CaCl₂ buffer at room temperature for 30 min with gentle mixing. The biotinylated anti-EGFR antibody was used at a 1:20 dilution ratio under similar reaction condition. Streptavidin-coated Bio-Adembeads were used in all the cellular detection assays. The beads were centrifuged/washed $3 \times$ in $1 \times$ PBS/MgCl₂/CaCl₂ and diluted with DI water to a 1:10 ratio. 40 μ L of the diluted Adembeads were added to 90 μ L of anti-EGFR aptamer or antibody-bound cells and incubated at room temperature for an additional 30 min with gentle mixing. The samples with $\sim 1.68 \times 10^9$ Adembeads and $\sim 2.4 \times 10^5$ cancer cells were finally resuspended in 1 mL buffer prior to injecting into the microfluidics.

2.9. Western blot

Panc-1 and MiaPaCa-2 cells were homogenized in a radio-immunoprecipitation assay (RIPA) buffer (Thermo Fisher Scientific, #89901) containing protease and phosphatase inhibitors (Thermo Fisher Scientific, #A32959). The total protein concentration was estimated and 30 μ L (10 ng/ μ L) of the cell lysate were loaded and separated by SDS-PAGE before transferring to a nitrocellulose membrane (BioRad, #1620177). Membranes were incubated with primary mouse anti-EGFR antibody (BioLegend, #933901) at 1:1000 dilution and a secondary antibody, horseradish peroxidase-conjugated goat anti-mouse IgG at 1:1000 dilution (Thermo Fisher Scientific, #31430). As a protein loading control, a primary rabbit anti-GAPDH antibody at 1:1000 dilution (Abcam, #ab181602) and a secondary antibody, horseradish peroxidase-conjugated goat anti-rabbit IgG 1:1000 dilution (Thermo Fisher Scientific, #31460) was used. The antigen-antibody complexes were detected by the ECL system (Thermo Fisher Scientific, #32106). A pre-stained molecular weight marker was run in parallel to determine the molecular weight of the proteins (BioRad, #1610375).

2.10. Optical flow cytometry

Panc-1 and MiaPaCa-2 cells were grown to 80% confluence and treated with Trypsin to detach them from the tissue culture flask. The cell number and viability were counted as described previously. A streptavidin-phycoerythrin (SA-PE, Prozyme) fluorophore was used to label the biotinylated anti-EGFR aptamer and the antibody. Cells ($\sim 1 \times 10^6$) were first incubated with the fluorophore labeled aptamer (100 nM final concentration) or the antibody (1:20 dilution) in 100 μ L PBS/MgCl₂/CaCl₂ for 30 min at room temperature. The stained cells were subsequently washed $3 \times$ with 200 μ L of PBS/MgCl₂/CaCl₂, resuspended in 500 μ L of the same buffer, and analyzed using FACSCalibur (BD Biosciences). The flow cytometry data was analyzed using FlowJo

software (BD Biosciences).

3. Results and discussion

Several limitations today restrict the portability of FCMs. First, conventional optical-based FCMs require extensive sample preparation, such as cell lysis and/or matrix purification to properly detect cells/cell surface receptors (e.g., CD4, EGFR, EpCAM) from crude samples due to the substantial optical background that the matrix presents (Issadore et al., 2012; Reisbeck et al., 2016). Second, FCMs often use sheath fluid to center the analytes in the middle of the channel with laminar flow and hydrodynamic focusing. Lastly, the readout instrumentation requires complex optics, lasers, and photodetectors making it hard to directly translate to PoC settings. To enable PoC, *sample-to-answer* operation, we minimized the amount of sample preparation required without significantly affecting the throughput or sensitivity. We accomplished this objectively using two techniques: 1) switching from an optical-based to a magnetic-based readout, and 2) co-optimizing the size of the sensor to remove the need for sheath fluid while generating a complex signature that enables advanced signal processing techniques to improve the SNR.

3.1. Hydrodynamic focusing

The background signal in a MFC is near zero as biological samples intrinsically lack magnetic material (Gaster et al., 2009; Osterfeld et al., 2008) thus removing the need for purification steps. Rather than using magnetic guides to focus the cells over a small sensor (Helou et al., 2013; Loureiro et al., 2009b; Reisbeck et al., 2016), we use the microfluidic channel to confine the cells over a much larger sensor. Using a large sensor negatively impacts the sensitivity, but, more importantly, ensures that the flowing analytes always travel across the active sensing area removing the need for sheath flow and minimizing false negative events. As will be described later, the larger sensor enables a complex signature to be generated rather than a simple bipolar peak, as shown in Fig. 1.

To enable high throughput detection in this relatively small channel (120 μm) compared with other MFCs (Helou et al., 2013; Murali et al., 2016; Reisbeck et al., 2018, p. 22, 2016; Tang et al., 2019), the seal between the sensor and the microfluidic channel needed to be improved to increase the flow rate and subsequently pressure. We achieved good sealing by applying UV-ozone treatment prior to bonding the sensor chip with the PDMS, post-curing to improve the contact, and spring-clamping to mechanically intensify the sealing while maintaining the sensor reusability, as shown in Supplemental Fig. 7. We performed hydrodynamic analysis for several different sized MNPs to determine the optimal flow rate and magnetic field strength to balance the MNPs in the middle of the channel height. Many forces were considered, including the drag force, magnetic force, gravity, and particle-particle (or particle-substrate) interactions through Van der Waals, electro-repulsive, and Langevin forces. After careful analysis, it was determined that drag force is the major contributor to the MNP's movement in the microfluidic channel. A plot showing these forces as a function of MNP size is illustrated in Supplemental Fig. 8. The drag force is at least one order of magnitude larger than magnetic force for the largest MNP (M-450, 4.5 μm) with our pumping setup. When sub-micron-sized MNPs (Adembeads, 200 nm; Nanomag-D, 130 nm; and SHS-30, 40 nm) are considered, magnetic force becomes comparable to DLVO forces and Langevin force. Drag force was kept dominant over other forces to allow the sample to flow in the middle of the channel and thus extract multi-parametric information.

3.2. Magnetic signature

Based on the average magnetic field exerted on a GMR SV sensor (as described in the Materials and Methods), the position-dependent signal of an M-450 MNP located at the sensor surface was simulated and is illustrated in Fig. 2A and 2B. The magnetoresistive (MR) signal exhibits

a strong dependence on the y-position, while it is rather insensitive to the x-position. The signal induced across the x-axis of the sensor varies by only 5% from the center to the edge whereas the path along the y-axis of the sensor generates a complex, multi-peak waveform with 2 major peaks and 5 minor peaks due to the serpentine sensor geometry consisting of 6 sensor stripes. This is in significant contrast to the simple bipolar-peak signal from a conventional single-stripe sensor (Fig. 1B) that can easily be mistaken for noise resulting in a false negative (missed detection event). This unique property will be exploited later to improve the SNR through signal processing techniques.

To evaluate and characterize the GMR SV-based MFC, we measured commercial MNPs with hydrodynamic sizes varying from 30 nm to 4.5 μm . The pumping rate for all MNPs was 10 $\mu\text{L}/\text{min}$ through a $120 \times 25 \mu\text{m}^2$ channel. The smallest MNP, SHS-30, had no distinguishable signal (Fig. 2C), as expected from simulation (Supplemental Fig. 6), due to its small magnetic moment and the strong particle-particle repulsion that prevents aggregation. While we did see occasional signatures from the other sub-micron MNP, Bio-Adembead, these were likely aggregates – not signal from individual particles. On the other hand, the M-280 and M-450 MNPs induced many signals. The velocity of the M-280 is faster (due to using the same pumping rate) and the signature degrades into a bipolar peak while the M-450 demonstrates the complete signature due to the slower velocity. It should be noted that the M-280 does show the full characteristic signature at slower pumping rates, but this pumping rate was chosen to allow all particles to use the same magnetic field for fair comparison. Fig. 2D shows the average signal amplitude where an event is counted as anything larger than 5σ the noise level of a negative control ($0.1 \times \text{PBS}$) experiment. As expected, the smaller MNPs generated smaller signals. It should be noted that while the out-of-plane magnetic field can be increased further to improve the amplitude, it is a delicate balance because as little as a 5° tilt between the sensor and a magnet can saturate the sensors. Furthermore, the divergence of the magnetic field modulates the amplitude across the sensor array. As a result, only the sensors located in the middle of the array were used for this comparison.

We also varied the channel height and the out-of-plane field to balance the magnetic force and study the effect of flowing height on signal. For example, a 130 mT field was used for tall channels (40- μm) while 60 mT was used for 19- μm channels. The measured data from the M-450 MNPs is in excellent agreement with simulation (Supplemental Fig. 9), while the M-280 data deviated from the simulated values, likely due to aggregation and/or chaining. As expected, small channels ensure the close proximity of the MNPs; however, aggregation and clogging were issues for channel heights of less than 12 μm and widths less than 50 μm . As such, we implemented the taller channel for rigid analytes where the channel height is at least $2 \times$ larger than the MNPs or biomimetic constructs, and comparable channel height for cells that have more shape flexibility.

3.3. Time-of-flight measurements

Raw data with no signal processing was collected while flowing 4.5 μm MNPs. As can be seen in Fig. 3A, each sensor in the linearly spaced array shows a time-sequenced response as the MNPs pass over the sensors. From these data, both the intra-sensor ToF (time between peaks within a signature) and the cross-sensor ToF (time between signatures on adjacent sensors) can be calculated. The ToF data directly measures the analyte velocity and serves as a proxy of its size, and the amplitude of the signature can be used to retrieve the vertical position of the analyte from the simulation library (Supplemental Fig. 6). At the current sampling rate, this system can handle velocities up to 7 mm/s without distorting the signature shape. Thus, the ToF data enables the MFC to have multi-parameter analysis (e.g., height, velocity, # of MNPs) of the analyte to further aid in discrimination and reduce false positives by signal processing.

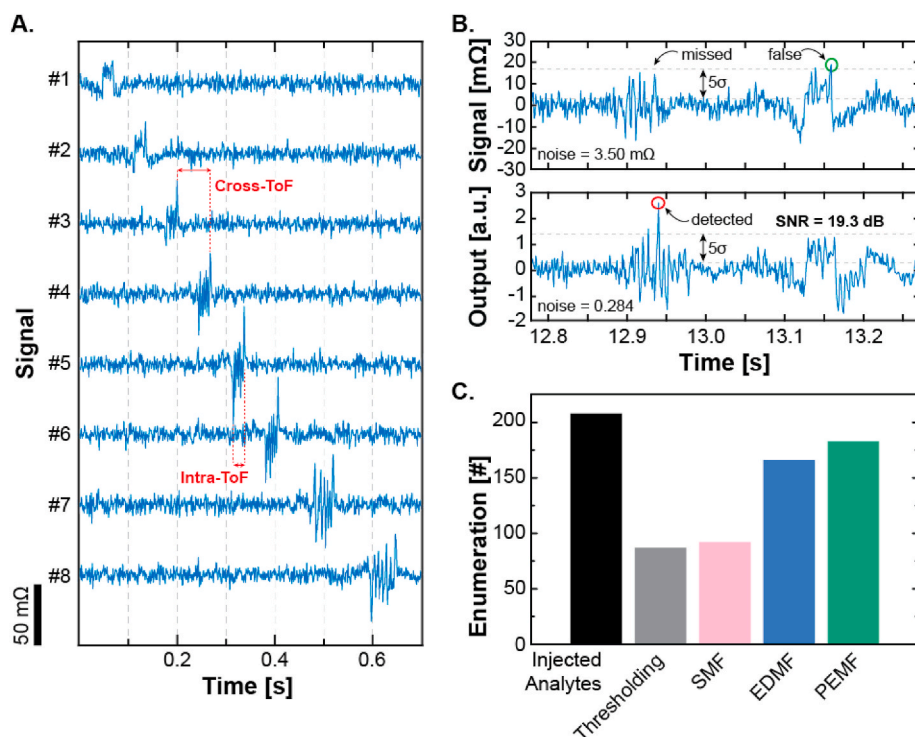


Fig. 3. A. Measured data from flowing 4.5- μm MNPs across the 1×8 sensor array exhibiting sequential signaling which enable ToF calculations and subsequent signal processing. B. Measured data of 4.5- μm MNPs showing missed detection using only raw-data thresholding and correct detection using matched filtering (PEMF). Thresholding was applied to both positive and negative signals although illustrated only on the positive side for clarity. C. Comparison of enumeration with biomimetic complexes using different signal processing techniques.

3.4. Matched filtering

Matched filtering was applied on the acquired data to improve the SNR and improve the detection efficiency (Huang et al., 2017a). By using a multi-stripe GMR SV configuration that creates a more complex signal, the benefit of matched filtering becomes more significant compared to many previous designs that used only a single stripe sensor resulting in a simple bipolar signature (Loureiro et al., 2009b). The complicated multi-peak signature here provides a more reliable and robust matching sequence reducing the minimum detectable SNR from 14 to 2.5 dB. Fig. 3B shows a snippet of measured data where simple thresholding at 5σ (SNR = 14 dB) results in missing the event; however, when applying matched filtering, the event is clearly visible at 12.95 s. Also shown is a motion artifact caused by a large impulse response at 13.15 s that would be counted as a false detection with thresholding. However, since this impulse does not possess a signal-like signature, the matched filtered output is kept within the 5σ threshold and it is correctly rejected.

Three types of matched filters were evaluated: simulation-based matched filters (SMF), energy-detection matched filters (EDMF), and previous-event matched filters (PEMF). The SMF looks for measured data with a similar pattern to those in a pre-computed simulation library based on Eq. (8). The EDMF template quantizes the expected signature into a tertiary square waveform: a positive level, a zero level, and a negative level. The tertiary template creates rectangular notches in a range where peaks are expected to be, roughly matching the waveform in a low-resolution fashion, and allowing for tolerance in peak position. By arranging the levels in a pattern that corresponds to the expected pattern, the filter finds expected peaks while normalizing the expected peak values to minimize that degree of uncertainty. The PEMF uses signatures from upstream (i.e. a previous sensor) recorded events. We apply thresholding (with a very low threshold, less than 5σ , often closer to 2σ) to all sensors to search for events. This is not limited to just sensor 1, we do this on all sensors to look for incoming events and propagate them downstream to the other sensors. One could also consider propagating upstream, but we found that this did not have a significant impact. After finding the signal sequence on any of the other sensors, the

detected signature is used as a template to compare against all other sensors for correlation within a time window based on the flow rate. In a relatively short time window, the flow rate, MNP distance to the sensor, and other slowly changing environmental parameters can be regarded as constant. Therefore, each of the sensors produces their own signature but delayed in time based on the velocity. An event is claimed if the matched filter output exceeds the threshold, which was set as 5σ . A majority voting algorithm with the eight sensors is used to reduce uncorrelated noise and declare a detection event.

Each of these matched filter templates has advantages and disadvantages. For example, owing to variation in particle size, even with the same pumping rate, particles can move at varying speeds, creating differences in the length of the target event waveform. The SMF struggles with intricate time warping between the measured signal and the template signal. In this case each peak start and end time could be slightly off from the template waveform, creating a complex warp from target to template where some areas of the signal are stretched and compressed at different rates. To deal with general differences in waveform size, we expanded the SMF library with a linear succession of filter lengths to discover each specific time variation. Stretching to different times required down-sampling or up-sampling. However, this increases the computation time significantly as the library expands. Alternatively, more advanced signal processing techniques, such as dynamic time warping (DTW) (Begum et al., 2015; Mueen and Keogh, 2016; Vullings et al., 1998), could be explored to solve the stretching issue with the SMF and potentially improve the system in the future. The EDMF is elegant in that it is essentially just looking for the coarse pattern but does not have significant improvement in the counting efficiency. Time variations were much easier to tolerate because waveform integrity was not as important for what is essentially a complex square signal. Since peaks were already being detected in a range of times rather than at a specific time, the malleability of the template proved to be much more useful than using a simulated template. Though EDMF has more flexibility in time warping and shape distortion than SMF, the velocity must be restricted to keep the intact or semi-intact complex signature. The PEMF is much more tolerant of dynamic changes in velocity and intrinsically outputs the ToF information. The enumeration efficacy using different

signal processing techniques can be seen in Fig. 3C. Some missing events can be attributed to temporal readout limitations when multiple beads/cells flowed over the sensor at the same time convoluting the signature. The PEMF outperforms the other techniques and is used for the remainder of this work.

3.5. Optical microscopy correlation

To evaluate the efficacy and quantify the accuracy, we correlated the measured electrical signal with video recorded by an optical microscope while flowing biomimetic complexes (10- μm polystyrene spheres decorated with Adembeads) and M-450 MNPs over the sensors. The Adembeads were chosen because they did not produce significant signal when not aggregated allowing differentiation between analytes bound with MNPs and unbound MNPs. Fig. 4 shows the recorded electrical signal alongside the optical images at the same timestamps. The cross-ToF was 79 ms while travelling from sensor 3 to 4 and 78 ms from sensor 4 to 5. The intra-sensor ToF can also be extracted from the time span between two edge-peaks within a sensor, resulting in a velocity of 5.09 mm/s. The PEMF excluded the fast-flowing Adembeads and clusters based on their velocity and magnetic signature. The counting efficiency was compared between thresholding (5σ) and the PEMF using the optical counting as the ground truth (Fig. 4B). For M-450, both

techniques have similar efficacy with detection rates of 80.62% and 92.25% for thresholding and the PEMF, respectively. However, for biomimetic MNP-decorated polymer spheres, thresholding only achieves a detection rate of 43.35% compared to the 88.18% with matched filtering. This is likely due to the complex sample which contains both biomimetic spheres, individual MNPs, and clusters of MNPs. The matched filter correctly rejects the latter two whereas thresholding cannot differentiate. The OM correlation reinforces the results shown in Fig. 3C that matched filtering exhibits strong reliability when introducing a complicated matrix. Notably, when using only one sensor of the array, the counting efficiency dropped from 80% to 43% for EDMF and from 44% to 23% for SMF. These data demonstrate the value in having an array of sensors compared to just a single sensor in improving the counting accuracy.

Receiver operator characteristic (ROC) curves were generated by sweeping the detection threshold to quantify the sensitivity and specificity of the proposed system. To establish ground truth, the flowing particles were analyzed frame-by-frame in ImageJ with size-based discrimination. Using just thresholding, the ROC curve lies very close to the random guess/chance curve, as shown in Fig. 4C. Applying the PEMF, the detection accuracy ($= \frac{\text{true positive} + \text{true negative}}{\text{number of events}}$) improved significantly, up to 83.68% for M-450 and 95.26% for biomimetic complexes

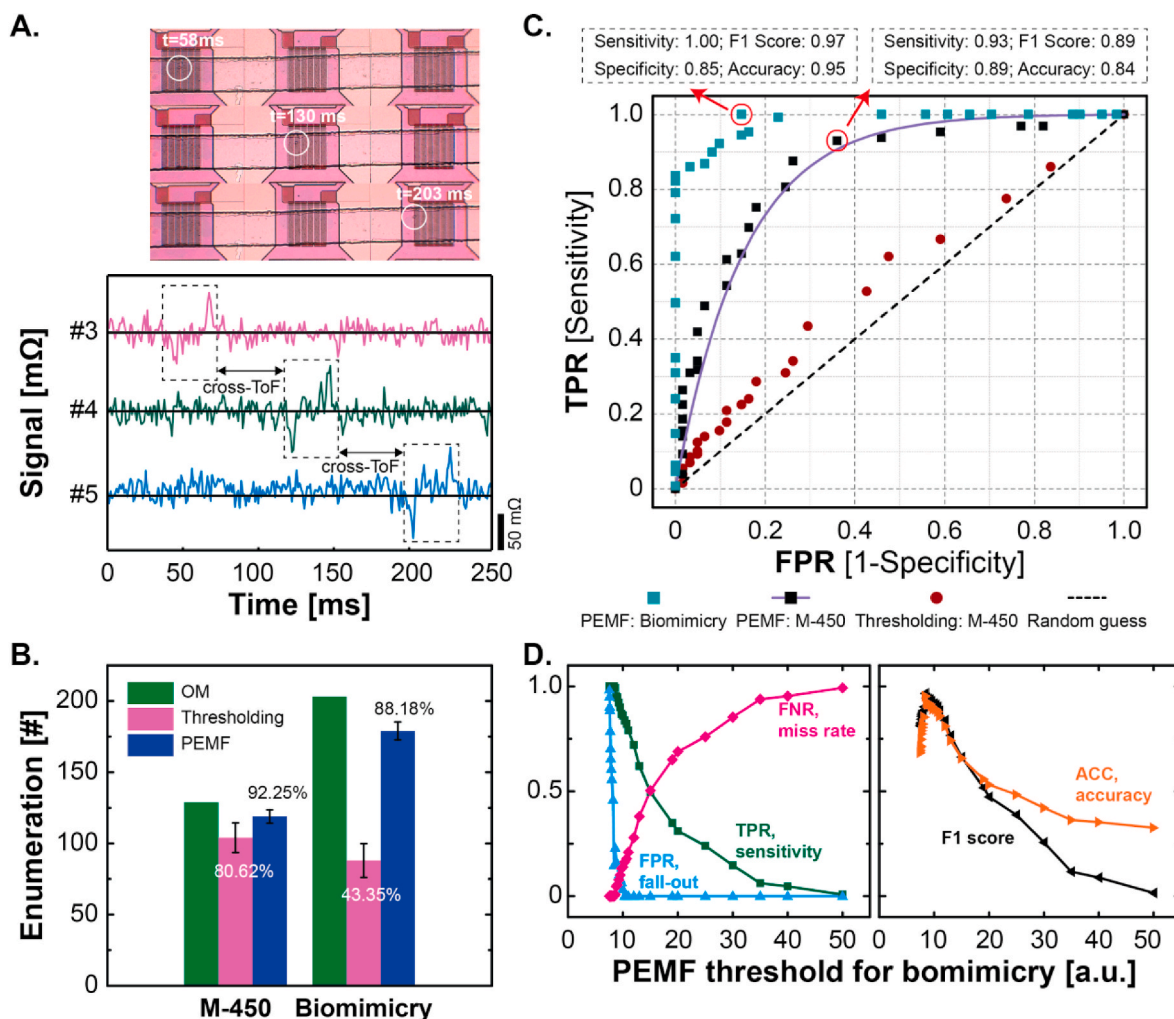


Fig. 4. A. Measured real-time data of OM-monitored sensors which enable ToF measurements. B. Compiled event-counting data. C. ROC curve of the selected sensor where green dots are the biomimicity data analyzed by matched filtering, square dots with the asymptote (purple curve) are the M-450 data analyzed by matched filtering, red dots are analyzed by thresholding from real-time data, and the grey dashed line is the random guess. D. Tradeoff between detection and thresholds, the highest accuracy happened when threshold was set at 8.4. (For interpretation of the references to color in this figure legend, the reader is referred to the Web version of this article.)

clearly demonstrating the benefit of matched filtering. Different from the correlation rate in Fig. 4B, which was only considered the positive samples with rigid thresholds (5σ), the ROC curve reveals the tradeoff between sensitivity and specificity for a system. As shown in Fig. 4D, increasing the PEMF threshold improved the false negatives, while the sensitivity and false positives were reduced simultaneously. The system achieved the best accuracy with a PEMF threshold of 8.4 compared to the 5σ ($= 9.6$) used in thresholding. This threshold strikes a balance between positive samples and negative samples but can be tuned based on the application.

3.6. Aptamer-based detection of pancreatic cancer cells

To establish the utility of the MFC in a cell detection assay, we used pancreatic cancer cell lines, Panc-1 and MiaPaca-2, that overexpress epidermal growth factor receptor (EGFR) on the cell surface. The Panc-1 cells had a $19.51 \mu\text{m}$ mean diameter (Supplemental Fig. 10). Therefore, we used the $20\text{-}\mu\text{m}$ -microfluidics channel height that is close to the size of the Panc-1 cells. A 5'-biotinylated 2'-fluoropyrimidine modified RNA aptamer (E07) that binds to EGFR with high affinity and specificity was used for the cell-labeling reaction (Ray et al., 2012). We also used, a biotinylated anti-EGFR antibody as an additional cancer cell staining reagent. Western blot and optical FCM were used to verify the surface expression of EGFR on the pancreatic cancer cell lines. Panc-1 cells expressed more EGFR compared to the MiaPaca-2 cells as detected by both the western blot and optical FCM results (Supplemental Figs. 11–12).

Panc-1 cells were conjugated with the biotinylated anti-EGFR aptamer and subsequently with the streptavidin-coated MNPs. This complex was then injected into the microfluidic channel and measurements were collected at $0.1 \mu\text{L}/\text{min}$ of throughput. As a negative control, we also injected PBS buffer, the MNPs alone, Panc-1 cells, and a mixture of MNPs and Panc-1 cells (without the aptamer linkers). In Fig. 5A and 5B, little to no counted events were detected in the PBS buffer ($n = 0$),

the Panc-1 cells ($n = 0$), or MNPs ($n = 38$) using the PEMF. A small number of counted events ($n = 769$) were detected in the Panc-1 and MNP mixture (without the biotinylated E07 aptamer linker), likely due to nonspecific binding on the cell surface from extremely excessive MNPs. However, in the presence of biotinylated E07 aptamer linker, the counted events increased nearly tenfold up to 7,140 per $5 \mu\text{L}$ in the Panc-1-E07-MNP mixture. To assess the throughput performance, we varied the flow rate of the Panc-1-E07-MNP complex in culture media (Supplemental Fig. 13). The data was collected at rates from 0.1 to $50 \mu\text{L}/\text{min}$, indicating the successful enumeration across two decades of throughput ($37 - 2730$ cells/min). This design with small channel heights performed well for MNPs and cells in PBS and cell culture media; however, it may need to be enlarged for serum due to cell aggregation resulting in clogging (Momen-Heravi et al., 2012).

Lastly, we compared the MFC and optical FCM data, shown in Fig. 5C. Mean fluorescence intensity (MFI) was calculated from the histogram plots of the optical flow cytometry data, and plotted against the mean magnetic intensity (MMI) values that were measured from the peak amplitudes of MFC data in each detected event. A very high correlation was obtained between the two flow cytometer sensing modalities ($R^2 = 0.98$). In addition, quantification of the bound MNPs can be derived from the MMI simulation (Supplemental Fig. 14) that indicates the amount of bound MNPs in the presence of anti-EGFR-antibody is in the range around 10^4 per cell. Notably, the difference in the protein expression of EGFR on the cell surface of these two cell lines, Panc-1 and MiaPaca-2, were also reflected in the MFC data obtained by using two different linkers, the anti-EGFR aptamer and antibody. Taken together, the data validates our proposed method against an optical FCM that is regarded as the gold-standard instrument.

3.7. Comparison

There has been significant interest in MFCs over the past decade, as shown in Table 1. Most prior MFCs have used high cross-sectional area

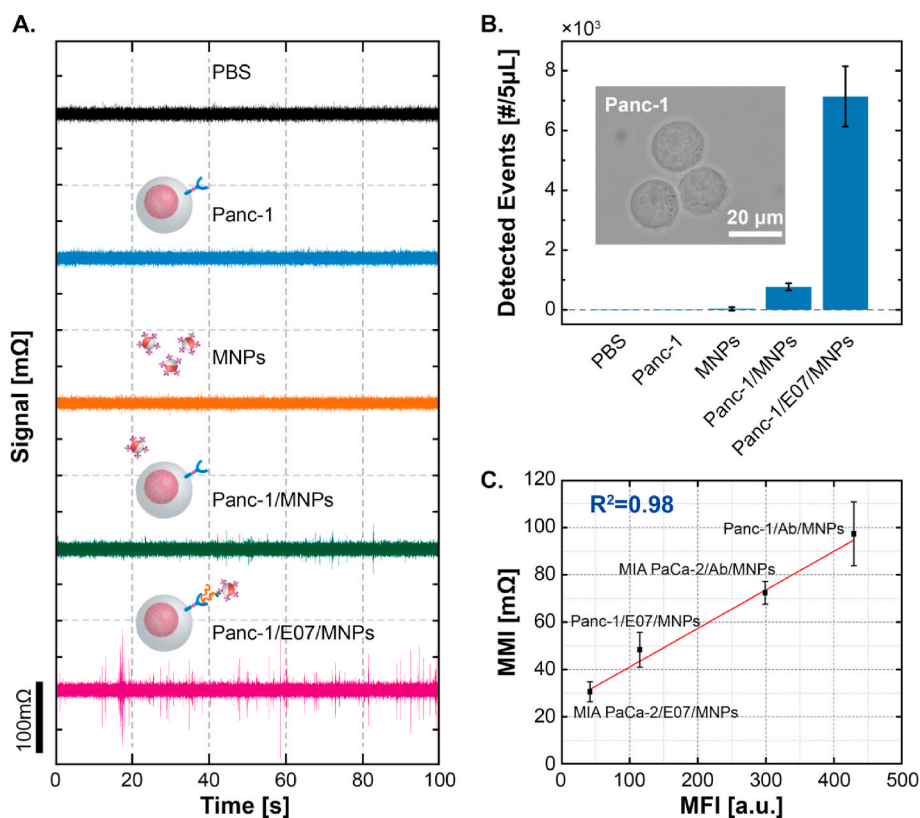


Fig. 5. A. Real-time measurements of Panc-1 model study using E07 aptamer. B. Enumeration plot calculated from MFC measurements, and the inset shows the visualized Panc-1 cells captured by microscope. C. Correlation between mean magnetic intensity (MMI) and mean fluorescence intensity (MFI) with different linkers, anti-EGFR antibody (shown as Ab) and E07 aptamer, and pancreatic cancer cell lines, Panc-1 and MIA PaCa-2. The error bars represent the counting difference throughout the measurements across 8 sensors.

Table 1
Comparison of published magnetic flow cytometers (MFCs).

		Lab Chip '11	Sci. Transl. Med. '12	Lab Chip '13	SREP '16	JSSC '17	Biosens. Bioe. '18	CICC '19	This work
Device & System	Sensor	GMR	μ Hall	GMR	GMR	spiral transformer	GMR	LC oscillator	GMR SV
	Sensor size ($w \times l$, μm^2)	3×40	8×8	2×30	2×30	$\sim 35 \times 50$	2×30	160 (diameter)	120×120
	Sensor configuration	single-stripe	cross	Wheatstone bridge	Wheatstone bridge	planar coil	Wheatstone bridge	planar coil	multi-stripe
	Array size	1×3	2×4	1×4	single sensor	1×4	single sensor	7×7	1×8
	Bead size	50 nm	10, 12, 16 nm 3, 8 μm	200 nm 12 μm	50, 200 nm 4, 6, 8, 12 μm	1, 4.5 μm	6, 8, 12 μm	2.8, 3 μm	200 nm $1, 2.8, 4.5 \mu\text{m}$
Microfluidics	Dimension ($w \times h$, μm^2)	150×14	125×25	700×200	700×150	200×100	1500×150 1500×300	60000	$90 \times 14 - 120 \times 40$
	Focusing technique	sheath	sheath	magnetic	magnetic	sheath	magnetic	–	laminar
Throughput	Flow Rate ($\mu\text{L}/\text{min}$)	1.26	1.67 – 16.67	24 – 60	60	2.5	72 – 90	36	0.1 – 50
	Throughput (cells/min)	~ 1400	N/A	60	N/A	500	N/A	N/A	37 – 2730
	Theoretical max ^a (cells/min)	N/A	$\sim 10^7$	N/A	N/A	N/A	N/A	N/A	$\sim 2 \times 10^6$
Signal	Signal processing	peak thresholding	N/A	peak thresholding	peak integral	matched filtering	peak integral	cross-correlation	matched filtering, cross-correlation
	OM correlation	–	–	Yes	Yes	–	Yes	Yes	Yes
Performance	Detection efficiency	N/A	N/A	N/A	N/A	74% – 87%	N/A	N/A	92.25%^b 88.18%^c
	Accuracy	N/A	0.96	N/A	N/A	N/A	N/A	N/A	83.68%^b 95.26%^c

^a (sampling rate) \times (samples/event).

^b Measured with Dynabeads M-450.

^c Measured with biomimetic polymer microsphere.

to surface area ratio microfluidics ($\frac{\text{Cross-sectional Area}_{\text{fluidics}}}{\text{Surface Area}_{\text{sensor}}} > 10$) to achieve high throughput (Fernandes et al., 2014a; Helou et al., 2013; Lin et al., 2014b, 2014a; Murali et al., 2016; Reisbeck et al., 2018, 2016; Vila et al., 2014). However, since the magnetic signal relies on the proximity to the sensing region (inversely proportional to the distance cubed), this is not typically a favorable design decision. As such, high area-ratio microfluidic setups lose most signals when MNP-decorated analytes flow near the middle of channel height compared to near the sensor surface. Some prior work have used magnetic chevrons (Helou et al., 2013; Reisbeck et al., 2018, 2016) or electrical current lines (Loureiro et al., 2009a) to guide the MNPs, which are close to the bottom of the channel, over the sensors and jetted successively to roll over the designated sensor area. Magnetic guides do improve the detection efficiency by focusing the analytes, however, they typically need slower flow rates which decreases the throughput and is prone to clogging. Another approach uses a strong magnetic field to attract the flowing MNP-decorated analytes near to the sensor surface, but the trajectory path makes signal modelling hard to translate into multi-parametric information and only allows binary outcomes. Furthermore, the trade-off between forces acting in the microfluidics is complicated when using high throughput, and this kind of force analysis was mostly done for magnetic sorting (De Palma et al., 2007; Liu et al., 2009; Wirix-Speetjens et al., 2005). As such, prior MFCs have not had high detection efficiency and high throughput as needed for rare-cell detection (e.g., circulating tumor cells). Considering the sensor design, miniaturization improves the sensor sensitivity, but the traditional single-stripe sensor geometry gives rise to the simple bipolar peak which is hard to differentiate signals from the noise in low SNR settings. While matched filtering has been utilized previously in an MFC (Murali et al., 2016), the spiral transformer generates a relatively low entropy signal (square wave) similar to the EDMF, which had lower performance than the PEMF in our measurements. To address these, we developed a GMR SV-based MFC and used matched filtering to recover the sensitivity and improve the specificity. This platform uses a multi-stripe GMR SV sensor with a large

active area and serpentine geometry that results in a unique signature. Our work demonstrates that the accuracy can be up to 95% in complex sample while the throughput strides two decades that fits the clinical need. We attribute the high detection efficiency and accuracy to the usage of a complex signature which increases the performance of the matched filtering as well as the redundancy afforded using an array of sensors.

4. Conclusion

In this work, we developed a GMR SV-based MFC that innovates and evolves key areas of cellular detection related to system design and signal processing. The micromagnetic simulation and hydrodynamic force study were performed to assess the fluidics design to maximize signal. Several commercial-available MNPs were measured and compared with the 200-nm MNPs selected for biomimetic model and cellular measurements. We demonstrated the improvement in SNR when applying matched filtering and compared different template functions. The PEMF exhibited a 5.6 \times improvement in the minimum SNR requirement and performed significantly better than traditional thresholding in terms of enumeration. Measurement results were compared with OM-monitored enumeration achieving detection efficiencies of 92% in the bead-only assay and 88% in the biomimetic assay. ROC analysis showed the sensitivity and specificity tradeoff achieving an accuracy of up to 95% for the model system. To lay the foundation for rapid cancer cell detection, we used an EGFR-targeting aptamer and detected pancreatic cancer cells across two decades of throughput. The MFC was compared against an optical FCM, the gold standard in cellular assay, demonstrating high correlation (98%). The GMR-SV-based MFC using matched filtering showed excellent performance with biomimetic model and aptamer-decorated cancer cellular detection in PBS. Future efforts will include evaluating DTW to improve the temporal restriction of signal processing. The design strategy of microfluidics and signal processing can be evolved in the future to address the challenges in biological sample (e.g. serum, whole blood) with varying applications (e.

g. high-throughput rare cell detection). Conclusively, this work lays the foundation for the proposed PoC “sample-to-answer” platform needed for NCD control and has the potential to meet the criterion of accuracy in clinical medical devices with advanced signal processing and microfluidics.

Declaration of competing interest

The authors declare the following financial interests/personal relationships which may be considered as potential competing interests: D. A.H. has related patents or patent applications assigned to Stanford University and out-licensed for potential commercialization. D.A.H. has stock in MagArray, Inc. and Flux Biosciences, which have licensed relevant patents from Stanford University for commercialization of GMR biosensor chips. All other authors declare no competing interests.

CRedit authorship contribution statement

Chih-Cheng Huang: Conceptualization, Methodology, Investigation, Writing - original draft, Visualization. **Partha Ray:** Investigation, Resources, Writing - review & editing. **Matthew Chan:** Software, Formal analysis. **Xiahn Zhou:** Resources, Formal analysis. **Drew A. Hall:** Conceptualization, Writing - review & editing, Supervision, Project administration, Funding acquisition.

Acknowledgements

This work was supported in part by the National Science Foundation (Grant ECCS-1454608) and Qualcomm.

Appendix A. Supplementary data

Supplementary data to this article can be found online at <https://doi.org/10.1016/j.bios.2020.112362>.

References

- Afsahi, S., Lerner, M.B., Goldstein, J.M., Lee, J., Tang, X., Bagarozzi, D.A., Pan, D., Locascio, L., Walker, A., Barron, F., Goldsmith, B.R., 2018. Biosens. Bioelectron. 100, 85–88.
- Aronoff-Spencer, E., Venkatesh, A.G., Sun, A., Brickner, H., Looney, D., Hall, D.A., 2016. Biosens. Bioelectron. 86, 690–696.
- Begum, N., Ulanova, L., Wang, J., Keogh, E., 2015. Accelerating dynamic time warping clustering with a novel admissible pruning strategy. In: Proceedings of the 21th ACM SIGKDD International Conference on Knowledge Discovery and Data Mining, KDD '15. Association for Computing Machinery, Sydney, NSW, Australia, pp. 49–58.
- Bhavnani, S.P., Narula, J., Sengupta, P.P., 2016. Eur. Heart J. 37, 1428–1438.
- Bompiani, K.M., Monroe, D.M., Church, F.C., Sullenger, B.A., 2012. J. Thromb. Haemostasis 10, 870–880.
- Cossarizza, A., Chang, H.-D., Radbruch, A., Akdis, M., Andrä, I., Annunziato, F., Bacher, P., Barnaba, V., Battistini, L., Bauer, W.M., Baumgart, S., Becher, B., Beischer, W., Berek, C., Bianco, A., Borsellino, G., Boullais, P.E., Brinkman, R.R., Büscher, M., Busch, D.H., Bushnell, T.P., Cao, X., Cavani, A., Chattopadhyay, P.K., Cheng, Q., Chow, S., Clerici, M., Cooke, A., Cosma, A., Cosmi, L., Cumano, A., Dang, V.D., Davies, D., Biasi, S.D., Zotto, G.D., Bella, S.D., Dellabona, P., Deniz, G., Dessing, M., Diefenbach, A., Santo, J.D., Dieli, F., Dolf, A., Donnenberg, V.S., Dörner, T., Ehrhardt, G.R.A., Endl, E., Engel, P., Engelhardt, B., Esser, C., Everts, B., Dreher, A., Falk, C.S., Fehniger, T.A., Filby, A., Fillatreau, S., Follo, M., Förster, I., Foster, J., Foulds, G.A., Frenette, P.S., Galbraith, D., Garbi, N., Garcia-Godoy, M.D., Geginat, J., Ghoreschi, K., Gibellini, L., Goettlinger, C., Goodyear, C.S., Gori, A., Grogan, J., Gross, M., Grützkau, A., Grummitt, D., Hahn, J., Hammer, Q., Hauser, A. E., Haviland, D.L., Hedley, D., Herrera, G., Herrmann, M., Hiepe, F., Holland, T., Hombrink, P., Houston, J.P., Hoyer, B.F., Huang, B., Hunter, C.A., Iannone, A., Jäck, H.-M., Jávega, B., Jonjic, S., Juelke, K., Jung, S., Kaiser, T., Kalina, T., Keller, B., Khan, S., Kienhöfer, D., Kromeis, K., Kunkel, D., Kurts, C., Kvistborg, P., Lannigan, J., Lantz, O., Larbi, A., LeibundGut-Landmann, S., Leipold, M.D., Levings, M.K., Litwin, V., Liu, Y., Lohoff, M., Lombardi, G., Lopez, L., Lovett-Racke, A., Lubberts, E., Ludewig, B., Lugli, E., Maecker, H.T., Marrtus, G., Matarese, G., Maueröder, C., McGrath, M., McInnes, I., Mei, H.E., Melchers, F., Melzer, S., Mielenz, D., Mills, K., Mirrer, D., Mjøsberg, J., Moore, J., Moran, B., Moretta, A., Moretta, L., Mosmann, T.R., Müller, S., Müller, W., Münz, C., Multhoff, G., Munoz, L.E., Murphy, K.M., Nakayama, T., Nasi, M., Neudörfl, C., Nolan, J., Nourshargh, S., O'Connor, J.-E., Ouyang, W., Oxenius, A., Palankar, R., Panske, I., Peterson, P., Peth, C., Petriz, J., Phillips, D., Pickl, W., Piconese, S., Pinti, M., Pockley, A.G., Podolska, M.J., Pucillo, C., Quataert, S.A., Radstake, T.R.D.

- J., Rajwa, B., Rebhahn, J.A., Recktenwald, D., Remmerswaal, E.B.M., Rezvani, K., Rico, L.G., Robinson, J.P., Romagnani, C., Rubartelli, A., Ruckert, B., Ruland, J., Sakaguchi, S., Sala-de-Oyaguren, F., Samstag, Y., Sanderson, S., Sawitzki, B., Scheffold, A., Schiemann, M., Schildberg, F., Schimisky, E., Schmid, S.A., Schmitt, S., Schober, K., Schüler, T., Schulz, A.R., Schumacher, T., Scotta, C., Shankey, T.V., Shemer, A., Simon, A.-K., Spidlen, J., Stall, A.M., Stark, R., Stehle, C., Stein, M., Steinmetz, T., Stockinger, H., Takahama, Y., Tarnok, A., Tian, Z., Toldi, G., Tornack, J., Traggiai, E., Trotter, J., Ulrich, H., Braber, M., van der Lier, van, R.A. W., Veldhoen, M., Vento-Asturias, S., Vieira, P., Voehringer, D., Volk, H.-D., Volkman, K., von, Waisman A., Walker, R., Ward, M.D., Warnatz, K., Warth, S., Watson, J.V., Watzl, C., Wegener, L., Wiedemann, A., Wienands, J., Willmsky, G., Wing, J., Wurst, P., Yu, L., Yue, A., Zhang, Q., Zhao, Y., Ziegler, S., Zimmermann, J., 2017. Eur. J. Immunol. 47, 1584–1797.
- De Palma, R., Liu, C., Barbagini, F., Reekmans, G., Bonroy, K., Laureyn, W., Borghs, G., Maes, G., 2007. J. Phys. Chem. C 111, 12227–12235.
- Fernandes, A.C., Duarte, C.M., Cardoso, F.A., Bexiga, R., Cardoso, S., Freitas, P.P., 2014a. Sensors 14, 15496–15524.
- Fernandes, E., Martins, V.C., Nóbrega, C., Carvalho, C.M., Cardoso, F.A., Cardoso, S., Dias, J., Deng, D., Kluskens, L.D., Freitas, P.P., Azeredo, J., 2014b. Biosens. Bioelectron. 52, 239–246.
- Freitas, P.P., Cardoso, F.A., Martins, V.C., Martins, S.A.M., Loureiro, J., Amaral, J., Chaves, R.C., Cardoso, S., Fonseca, L.P., Sebastião, A.M., Pannetier-Lecoq, M., Fermon, C., 2012. Lab Chip 12, 546–557.
- Gaster, R.S., Hall, D.A., Nielsen, C.H., Osterfeld, S.J., Yu, H., Mach, K.E., Wilson, R.J., Murmann, B., Liao, J.C., Gambhir, S.S., Wang, S.X., 2009. Nat. Med. 15, 1327–1332.
- Helou, M., Reisbeck, M., Tedde, S.F., Richter, L., Bär, L., Bosch, J.J., Stauber, R.H., Quandt, E., Hayden, O., 2013. Lab Chip 13, 1035–1038.
- Huang, C., Zhou, X., Ying, D., Hall, D.A., 2017a. A GMR-based magnetic flow cytometer using matched filtering. In: 2017 IEEE SENSORS. Presented at the 2017 IEEE SENSORS, pp. 1–3.
- Huang, C.-C., Zhou, X., Hall, D.A., 2017b. Sci. Rep. 7, srep45493.
- Issadore, D., Chung, J., Shao, H., Liang, M., Ghazani, A.A., Castro, C.M., Weissleder, R., Lee, H., 2012. Sci. Transl. Med. 4, 141ra92–141ra92.
- Jennings, C.D., Foon, K.A., 1997. Blood 90, 2863–2892.
- Jiang, H., Sun, A., Venkatesh, A.G., Hall, D.A., 2017. IEEE Sensor. J. 17, 589–597.
- Julius, M.H., Simpson, E., Herzenberg, L.A., 1973. Eur. J. Immunol. 3, 645–649.
- Kwon, L., Long, K.D., Wan, Y., Yu, H., Cunningham, B.T., 2016. Trends in vitro diagnostics and mobile healthcare. Biotechnol. Adv. 34, 291–304.
- Li, Guanxiang, Wang, S.X., 2003. IEEE Trans. Magn. 39, 3313–3315.
- Li, X., Dunn, J., Salins, D., Zhou, G., Zhou, W., Rose, S.M.S.-F., Perelman, D., Colbert, E., Runge, R., Rego, S., Sonecha, R., Datta, S., McLaughlin, T., Snyder, M.P., 2017. PLoS Biol. 15, e2001402.
- Lin, G., Makarov, D., Medina-Sánchez, M., Guix, M., Baraban, L., Cuniberti, G., Schmidt, O.G., 2014a. Lab Chip 15, 216–224.
- Lin, G., Makarov, D., Melzer, M., Si, W., Yan, C., Schmidt, O.G., 2014b. Lab Chip 14, 4050–4058.
- Lin, G., Karnaushenko, D.D., Bermúdez, G.S.C., Schmidt, O.G., Makarov, D., 2016. Small 12, 4553–4562.
- Liu, C., Stakenborg, T., Peeters, S., Lagae, L., 2009. J. Appl. Phys. 105, 102014.
- Loureiro, J., Fermon, C., Pannetier-Lecoq, M., Arrias, G., Ferreira, R., Cardoso, S., Freitas, P.P., 2009a. IEEE Trans. Magn. 45, 4873–4876.
- Loureiro, J., Ferreira, R., Cardoso, S., Freitas, P.P., Germano, J., Fermon, C., Arrias, G., Pannetier-Lecoq, M., Rivadulla, F., Rivas, J., 2009b. Appl. Phys. Lett. 95, 034104.
- Loureiro, J., Andrade, P.Z., Cardoso, S., Silva, C.L. da, Cabral, J.M., Freitas, P.P., 2011. Lab Chip 11, 2255–2261.
- Malcovati, L., Germing, U., Kuendgen, A., Della Porta, M.G., Pascutto, C., Invernizzi, R., Giagounidis, A., Hildebrandt, B., Bernasconi, P., Knipp, S., Strupp, C., Lazzarino, M., Aul, C., Cazzola, M., 2007. J. Clin. Oncol. 25, 3503–3510.
- Momen-Heravi, F., Balaj, L., Alian, S., Trachtenberg, A.J., Hochberg, F.H., Skog, J., Kuo, W.P., 2012. Front. Physiol. 3.
- Mueen, A., Keogh, E., 2016. Extracting optimal performance from dynamic time warping. In: Proceedings of the 22nd ACM SIGKDD International Conference on Knowledge Discovery and Data Mining, KDD '16. Association for Computing Machinery, San Francisco, California, USA, pp. 2129–2130.
- Murali, P., Niknejad, A.M., Boser, B.E., 2016. IEEE J. Solid-State Circuits, pp. 1–13.
- Osterfeld, S.J., Yu, H., Gaster, R.S., Caramuta, S., Xu, L., Han, S.-J., Hall, D.A., Wilson, R. J., Sun, S., White, R.L., Davis, R.W., Pourmand, N., Wang, S.X., 2008. Proc. Natl. Acad. Sci. 105, 20637–20640.
- Perfetto, S.P., Chattopadhyay, P.K., Roederer, M., 2004. Nat. Rev. Immunol. 4, 648–655.
- Ray, P., Cheek, M.A., Sharaf, M.L., Li, N., Ellington, A.D., Sullenger, B.A., Shaw, B.R., White, R.R., 2012. Nucleic Acid Therapeut. 22, 295–305.
- Reisbeck, M., Helou, M.J., Richter, L., Kappes, B., Friedrich, O., Hayden, O., 2016. Sci. Rep. 6, 32838.
- Reisbeck, M., Richter, L., Helou, M.J., Arlinghaus, S., Anton, B., van Dommelen, I., Nitzsche, M., Baßler, M., Kappes, B., Friedrich, O., Hayden, O., 2018. Biosens. Bioelectron. 109, 98–108.
- Rizzi, G., Lee, J.-R., Guldborg, P., Dufva, M., Wang, S.X., Hansen, M.F., 2017. Biosens. Bioelectron. 93, 155–160. Special Issue Selected Papers from the 26th Anniversary World Congress on Biosensors (Part II).
- Salvati, A., Nelissen, I., Haase, A., Åberg, C., Moya, S., Jacobs, A., Alnasser, F., Bewersdorff, T., Deville, S., Luch, A., Dawson, K.A., 2018. Nanolmpact 9, 42–50.
- Sun, A.C., Hall, D.A., 2019. Electroanalysis 31, 2–16.
- Tang, H., Venkatesh, S., Lin, Z., Lu, X., Saeidi, H., Rather, G.M., Bertino, J.R., Lin, C., Javanmard, M., Sengupta, K., 2019. 2D magnetic sensor array for real-time cell tracking and multi-site detection with increased robustness and flow-rate. In: 2019

- IEEE Custom Integrated Circuits Conference (CICC). Presented at the 2019 IEEE Custom Integrated Circuits Conference (CICC), pp. 1–4.
- United Nations, 2017. Department of Economics and Social Affairs, Population Division. World population ageing, 2017 highlights.
- Vashist, S.K., Lippa, P.B., Yeo, L.Y., Ozcan, A., Luong, J.H.T., 2015. Trends Biotechnol. 33, 692–705.
- Vila, A., Martins, V.C., Chícharo, A., Rodriguez-Abreu, C., Fernandes, A.C., Cardoso, F.A., Cardoso, S., Rivas, J., Freitas, P., 2014. IEEE Trans. Magn. 50, 1–4.
- Vullings, H.J.L.M., Verhaegen, M.H.G., Verbruggen, H.B., 1998. Automated ECG segmentation with dynamic time warping. In: Proceedings of the 20th Annual International Conference of the IEEE Engineering in Medicine and Biology Society. Vol.20 Biomedical Engineering towards the Year 2000 and Beyond (Cat. No.98CH36286). Presented at the Proceedings of the 20th Annual International Conference of the IEEE Engineering in Medicine and Biology Society. Vol.20 Biomedical Engineering Towards the Year 2000 and Beyond (Cat. No.98CH36286), vol. 1, pp. 163–166.
- Wang, Y.-L., Huang, C.-C., Kang, Y.-W., 2014. IET Nanobiotechnol. 8, 10–17.
- Wang, Y., Wang, W., Yu, L., Tu, L., Feng, Y., Klein, T., Wang, J.-P., 2015. Biosens. Bioelectron. 70, 61–68.
- Wannenburg, J., Malekian, R., 2015. IEEE Sensor. J. 15, 6839–6852.
- Williams, A.J., Cooper, W.M., Ramsaroop, S., Alusta, P., Buzatu, D.A., Wilkes, J.G., 2017. Front. Microbiol. 8.
- Wirix-Speetjens, R., Fyen, W., Xu, Kaidong, De Boeck, Jo, Borghs, G., 2005. IEEE Trans. Magn. 41, 4128–4133.
- World Health Organization, 2018. Noncommunicable Diseases Country Profiles 2018.
- Zhou, X., Huang, C., Hall, D.A., 2017. IEEE Trans. Biomed. Circuits Syst. 11, 755–764.
- Zhou, X., Sveiven, M., Hall, D.A., 2019a. IEEE Trans. Biomed. Circuits Syst. 13, 1254–1263.
- Zhou, X., Sveiven, M., Hall, D.A., 2019b. 11.4 A fast-readout mismatch-insensitive magnetoresistive biosensor front-end achieving sub-ppm sensitivity. In: 2019 IEEE International Solid-State Circuits Conference - (ISSCC), pp. 196–198.
- Zhu, H., Mavandadi, S., Coskun, A.F., Yaglidere, O., Ozcan, A., 2011. Anal. Chem. 83, 6641–6647.
- Zhu, H., Isikman, S.O., Mudanyali, O., Greenbaum, A., Ozcan, A., 2013. Lab Chip 13, 51–67.